

# Cosmology/COBE

EDWARD L. WRIGHT  
*UCLA Dept. of Astronomy*  
*Los Angeles CA 90024-1562*

## Abstract

The results from the *COBE*\*satellite are in close quantitative agreement with the predictions of the standard hot Big Bang model, suggesting that the Universe was once hot, dense and isothermal, giving a background radiation spectrum that is close to a perfect blackbody. The need to preserve this blackbody spectrum to match the spectrum observed by the FIRAS instrument on *COBE* places strong limits on events and scenarios occurring later than 1 year after the Big Bang. The observation of intrinsic anisotropy of the microwave background by the DMR instrument on *COBE* provides a measurement of the magnitude of the gravitational potential fluctuations that existed  $10^{5.5}$  years after the Big Bang. These potential perturbations were either produced in an inflationary epoch sometime during the first picosecond after the Big Bang, or else they are initial conditions dating from  $t = 0$ . The angular power spectrum of the correlations is compatible with the inflationary scenario. The observed amplitude of  $\Delta T$  can be used to restrict theories of the fundamental structure of matter on micro-physical scales and at energies higher than that of the most energetic cosmic rays. The gravitational forces implied by the observed potential can produce the observed clustering of galaxies, but only if the density of the Universe is dominated by some form of transparent “dark” matter, which interacts weakly with photons. While the FIRAS and DMR instruments have  $7^\circ$  beams, the third instrument on *COBE*, DIRBE, has collected data with an  $0.7^\circ$  beam that will be used to improve our knowledge of the cosmic infrared background, but only after the strong foreground emissions from the interplanetary dust cloud and galactic dust are modeled and removed.

## 1. Introduction

The observables of modern cosmology include the Hubble expansion of the Universe; the ages of stars and clusters; the distribution and streaming motions

---

\* The National Aeronautics and Space Administration/Goddard Space Flight Center (NASA/GSFC) is responsible for the design, development, and operation of the Cosmic Background Explorer (COBE). Scientific guidance is provided by the COBE Science Working Group. GSFC is also responsible for the development of the analysis software and for the production of the mission data sets.

of galaxies; the content of the Universe (its mass density, composition, and the abundances of the light elements); the existence, spectrum and anisotropy of the cosmic microwave background radiation; and other potential backgrounds in the infrared, ultraviolet, x-ray, and gamma-ray spectral regions. The purpose of the *COBE* mission is to make definitive measurements of two of these observable cosmological fossils: the cosmic microwave background (CMB) radiation and the cosmic infrared background (CIB) radiation. Since the discovery of the CMB<sup>1</sup>, many experiments have been performed to measure the CMB spectrum and spatial anisotropies over a wide range of wavelengths and angular scales. Fewer attempts have been made to conduct a sensitive search for a CIB radiation, expected to result from the cumulative emissions of luminous objects formed after the universe cooled sufficiently to permit the first stars and galaxies to form.

The three scientific instruments on *COBE* are the Far Infrared Absolute Spectrophotometer (FIRAS), the Differential Microwave Radiometers (DMR), and the Diffuse Infrared Background Experiment (DIRBE). The purpose of FIRAS is to make a precision measurement of the spectrum of the CMB from 1 cm to 100  $\mu\text{m}$ . The purpose of DMR is to search for variations in the temperature of the CMB on angular scales larger than  $7^\circ$  at frequencies of 31.5, 53, and 90 GHz. The purpose of DIRBE is to search for a CIB by making absolute brightness measurements of the diffuse infrared radiation in 10 photometric bands from 1 to 240  $\mu\text{m}$  and polarimetric measurements from 1 to 3.5  $\mu\text{m}$ . The FIRAS and DIRBE instruments are located inside a 650 liter superfluid liquid helium dewar. See Boggess *et al.*<sup>2</sup> for a full description of the *COBE* mission.

The *COBE* mission is the product of many years of work by a large team of scientists and engineers. Credit for all of the results presented in this paper must be shared with the other members of the the *COBE* Science Working Group: Chuck Bennett, Ed Cheng, Eli Dwek, Mike Hauser, Tom Kelsall, John Mather, Harvey Moseley, Nancy Boggess, Rick Shafer, Bob Silverberg, George Smoot, Steve Meyer, Rai Weiss, Sam Gulkis, Mike Janssen, Dave Wilkinson, Phil Lubin, and Tom Murdock. Bennett *et al.*<sup>3</sup> is a review of the history of the *COBE* project and its results up to the discovery of the anisotropy by the DMR, but not including the latest FIRAS limits on distortions.

Some of the members of this team have been working on *COBE* since the release of the NASA Announcement of Opportunities AO-6 and AO-7 in 1974, when the proposals for what became the *COBE* project were submitted. I have been working on *COBE* since the beginning of 1978. *COBE* was successfully launched at 14:34 UT on 18 November 1989 from Vandenberg AFB, California, and returned high quality scientific data from all three instruments for ten months until the liquid helium ran out. But about 50% of the instruments do not require liquid helium, and are still returning valuable scientific data in July 1993. While the *COBE* mission has been

successful, making the “discovery of the century”, one must remember that this work is based on the earlier work (in the 20<sup>th</sup> century!) of Hubble<sup>4</sup> and Penzias and Wilson<sup>1</sup>, who discovered the expansion of the Universe and the microwave background itself. As a consequence of these two discoveries, one knows that the early Universe was hot and dense. When the density and temperature are high, the photon creation and destruction rates are high, and are sufficient to guarantee the formation of a good blackbody spectrum. Later, as the Universe expands and cools, the photon creation and destruction rates become much slower than the expansion rate of the Universe, which allow distortions of the spectrum to survive. In the standard model the time from which distortions could survive is 1 year after the Big Bang at a redshift  $z \approx 10^{6.4}$ .

However, the expansion of the Universe will not produce a distortion by itself, since adiabatically expanding a blackbody radiation field results in another blackbody with a lower temperature. Thus the existence of a distorted spectrum in the hot Big Bang model requires the existence at time later than 1 year after the Big Bang of both an energy source and an emission mechanism that can produce photons that are now in the millimeter spectral range. Conversely, a lack of distortions can be used to place limits on any such energy source, such as decaying neutrinos, dissipation of turbulence, etc.

At a time  $10^{5.4}$  years<sup>†</sup> after the Big Bang, at  $z \approx 1360$ , the temperature has fallen to the point where helium and then hydrogen have 50% (re)combined into transparent gases<sup>5</sup>. The surface of last scattering ( $\partial\tau/\partial\ln(1+z) = 1$ ) occurs later, at  $z \approx 1160$  or  $10^{5.7}$  years after the Big Bang. The electron scattering which had impeded the free motion of the CMB photons until this epoch is removed, and the photons stream across the Universe. Before recombination, the radiation field at any point was constrained to be nearly isotropic because the rapid scattering scrambled the directions of photons. The radiation field was not required to be homogeneous, because the photons remained approximately fixed in comoving co-ordinates. After recombination, the free streaming of the photons has the effect of averaging the intensity of the microwave background over a region with a size equal to the horizon size. Thus after recombination any inhomogeneity in the microwave background spectrum is smoothed out. Note that this inhomogeneity is not lost: instead, it is converted into anisotropy. When we study the isotropy of the microwave background, we are looking back to the surface of last scattering  $\approx 10^{5.5}$  years after the Big Bang. But the hot spots and cold spots we are studying existed as inhomogeneities in the Universe before recombination. Since the  $7^\circ$  beam used by the DMR instrument on *COBE* is larger than the horizon size at recombination, these inhomogeneities cannot be constructed in a causal fashion during the epoch before recombination in the standard Big Bang model. Instead, they must be installed “just so” in the initial

---

<sup>†</sup> With  $H_0 = 50$ ,  $\Omega = 1$ .

conditions. In the inflationary scenario<sup>6</sup> these large scale structures were once smaller than the horizon size during the inflationary epoch, but grew to be much larger than the horizon. Causal physics acting  $10^{-35}$  seconds after the Big Bang can produce the large-scale inhomogeneities studied by the DMR.

## 2. COBE Orbit and Attitude

*COBE* was launched at dawn on 18 November 1989 into a sun-synchronous orbit with an inclination of  $99^\circ$  and an altitude of 900 km. By choosing a suitable combination of inclination and altitude, the precession rate of the orbit can be set to follow the motion of the Sun around the sky at 1 cycle per year. Thus the line perpendicular to the orbit plane always points approximately toward the Sun. Since *COBE* was launched toward the South in the morning, the end of the orbit normal which points toward the Sun is at declination  $-9^\circ$ . At the June solstice, when the declination of the Sun is  $+23^\circ$ , there is a  $32^\circ$  deviation from the ideal situation where the Earth-Sun line is exactly perpendicular to the orbit. Since the depression of the horizon given by  $\cos d = R_\oplus/a$ , where  $a$  is the radius of the orbit of *COBE*, is  $29^\circ$ , there are eclipses when *COBE* passes over the South pole for a period of two months centered on the June solstice. During the same season at the North pole the angle between the Sun and anti-Sunward limb of the Earth is only  $177^\circ$ . It is thus not possible to keep both Sunlight and Earthshine out of the shaded cavity around the dewar. Since the Sun produces a much greater bolometric intensity than a thin crescent of Earth limb, the choice to keep the Sun below the plane of the shade is an obvious one.

The pointing of *COBE* is normally set to maintain the angle between the spin axis and the Sun at  $94^\circ$ . This leaves the Sun  $4^\circ$  below the plane of the shade. During eclipse seasons this margin is shaved to  $2^\circ$  to reduce the amount of Earthshine into the shaded cavity where the instruments sit. The angle between the plane of the shade and the Sun is known as the “roll” angle. The “pitch” angle describes the rotation of the spin axis around the Earth-Sun line. This rotation is programmed for a constant angular rate of 1 cycle per orbit. The nadir is set to be close to the minus spin axis, but because the Sun can be up to  $32^\circ$  from the orbit normal and the Sun is kept  $4^\circ$  below the plane of the shade, the spin axis can be up to  $36^\circ$  away from the zenith. The uniform rate in pitch allows the nadir to oscillate by up to  $\pm 6^\circ$  relative to the spin-Sun plane with a period of 2 cycles per orbit. This motion is similar to the effect of the inclination of the ecliptic on the equation of time that can be seen in an analemma. To keep the “wind” caused by the orbital motion of *COBE* from impinging on the cryogenic optics, the pitch is biased backward by  $6^\circ$ . The “yaw” motion of *COBE* is its spin. The spin period is about 73 seconds.

There are two types of instrument pointings on *COBE*. The DMR and DIRBE instruments have fields-of-view located  $30^\circ$  away from the spin axis. As a result they scan cycloidal paths through the sky, that cover the band from  $64^\circ$  to  $124^\circ$  from the Sun. This band contains 50% of the sky, and it is completely covered in a day by the DMR or DIRBE. This rapid coverage of the sky implies a rapid scan rate:  $2.5^\circ/\text{sec}$ . The data rates are also high: the DIRBE transmits 8 readings/channel/sec, while the DMR transmits 2 readings/channel/sec. The FIRAS points straight out along the spin axis. As a result its field-of-view moves only at the orbital rate of  $3.6^\circ/\text{min}$ . Since FIRAS coadds interferograms over a collection period of about 30 to 60 seconds, this slow scanning of the sky is essential.

Over the course of a year the Sun moves around the sky, and the scan paths of the instruments follow this motion. The leading edge of the wide scanned band for the DIRBE and DMR caught up to the trailing edge of the band at start of mission after 4 months, leading to 100% sky coverage. For the FIRAS total sky coverage would in principle be obtained after 6 months, but because of gaps in the observations caused by calibration runs and lunar interference, the actual sky coverage for FIRAS, defined as having the center of the beam within a pixel, is about 90%. The coverage gaps are sufficiently narrow, however, that every direction on the sky was covered by at least the half power contour of the beam.

The attitude determination system for *COBE* uses infrared star sightings from DIRBE to correct a gyro propagated attitude solution. This method requires 3 working gyros that are not co-planar. On 10 July 1993, *COBE* suffered its fourth gyro failure out of six gyros, which will degrade the accuracy of the attitude solutions by about a factor of 5, to a  $1\sigma$  accuracy of about  $0.1^\circ$ . (One of the failed gyros is noisy but operable.) This accuracy will be sufficient for the DMR experiment with its  $7^\circ$  beam, provided that the errors are not systematic. Current planning is to operate *COBE* until December 1993, which will complete four years of observations with the DMR and the short wavelength channels of the DIRBE.

### 3. DIRBE Measurements

The Diffuse Infrared Background experiment (DIRBE) on *COBE* is designed to search for a cosmic infrared background (CIB). Models of the CIB radiation take light from distant, unresolved galaxies, and redshift it into the near infrared bands<sup>7</sup>; or absorb the starlight on dust, reradiate it in the far-infrared, and then redshift it into the sub-millimeter band<sup>8</sup>. These models predict fluxes that are approximately two orders of magnitude lower than the emission from the Milky Way, which makes detection of the CIB a difficult task, unless observations are made at wavelengths where the redshift carries the energy from distant galaxies into a region with little

Milky Way emission. The interplanetary dust cloud, which scatters sunlight to give the zodiacal light, absorbs much more power than it scatters and reradiates this power in the mid-infrared. Thus from  $5 \mu\text{m}$  to  $100 \mu\text{m}$  the CIB is overwhelmed when observing from a distance 1 au from the Sun. However, there are windows between the scattered and thermal zodiacal light at  $3.5 \mu\text{m}$  and between the interstellar dust in the Milky Way and the CMBR at 200-300  $\mu\text{m}$  where the CIB may be detectable.

The DIRBE instrument is an off-axis Gregorian telescope with a 19 cm diameter primary. The Gregorian design has an intermediate image of the sky, which allows for the placement of a stray-light stop between the primary and the secondary, and the secondary forms an image of the primary where a second stray-light stop is located. Baffle vanes in the telescope tube absorb radiation coming from far off-axis, so the main path for stray light involves scattering on the primary mirror when it is illuminated by a slight off-axis source. Great care was taken to avoid contamination and to preserve the cleanliness of the optics, so the off-axis response of the DIRBE is very small. The DIRBE beam is an  $0.7^\circ \times 0.7^\circ$  square. Dichroics and aperture division are used to give simultaneous measurements in 10 spectral bands in the same field of view. The 10 bands in DIRBE are the ground-based photometry bands J[1.2], K[2.3], L[3.4], and M[4.9]; the four IRAS bands at 12, 25, 60, and 100  $\mu\text{m}$ ; and two long wavelength bands at 140 and 240  $\mu\text{m}$ . The shortest wavelengths (JKL) bands, which observe scattered light from the interplanetary dust cloud, have 3 detectors per band with polarizers to measure linear polarization. A tuning fork running at 32 Hz serves as a chopper for the DIRBE. This gives a well-determined zero level by comparing the sky signal to the 2 K interior of the DIRBE, allowing the search for an isotropic CIB to proceed. A shutter blocks the optical path less frequently, so the accuracy of the zero level can be checked. When the shutter is in the beam, its back side is a mirror which reflect light from a commandable internal reference source (IRS) into the detectors, providing a gain calibration several times per orbit. During the 10 months of cryogenic operation, the achieved instrument rms sensitivity per field of view was  $\lambda I(\lambda) = (1.0, 0.9, 0.6, 0.5, 0.3, 0.4, 0.4, 0.1, 11.0, 4.0) \times 10^{-9} \text{ W m}^{-2} \text{ sr}^{-1}$ , respectively for the ten wavelength bands listed above. These noise levels are considerably smaller than the total fluxes measured by DIRBE at the South Ecliptic Pole given in Table 1. Note that the predicted extragalactic flux is  $3 \times 10^{-8} \text{ W m}^{-2} \text{ sr}^{-1}$  at both  $3.5 \mu\text{m}^7$  and  $240 \mu\text{m}^8$ , which is 20% of the total SEP flux at  $3.5 \mu\text{m}$  and 43% at  $240 \mu\text{m}$ .

The final determination of the magnitude of the extragalactic background will depend on modeling and removing the zodiacal light. The DIRBE beam is aligned  $30^\circ$  from the spin axis of *COBE*, so it swings from  $64^\circ$  elongation to  $124^\circ$  elongation in every rotation of the satellite. In principle, the variation of intensity with elongation can be used to determine the magnitude of the zodiacal emission, just as the variation of atmospheric extinction with secant of the zenith angle allows one to determine the flux hitting the top of the atmosphere. However, the shape of the atmosphere is well

Reference	$\lambda$ ( $\mu\text{m}$ )	$\lambda I_\lambda$ ( $10^{-7} \text{ W m}^{-2} \text{ sr}^{-1}$ )	$T_B(\lambda)$ K
DIRBE ( <i>South Ecliptic Pole</i> )	1.2	$8.3 \pm 3.3$	351
	2.3	$3.5 \pm 1.4$	216
	3.4	$1.5 \pm 0.6$	140
	4.9	$3.7 \pm 1.5$	109
	12.	$29. \pm 12$	56
	22.	$21. \pm 8$	34
	55.	$2.3 \pm 1$	15
	96.	$1.2 \pm 0.5$	9.2
	151.	$1.3 \pm 0.7$	6.6
	241.	$0.7 \pm 0.4$	4.5

Table 1: Brightness and Planck Brightness Temperature of the Diffuse Infrared Sky

known, while the shape of the zodiacal dust cloud is poorly determined. If the cloud is in equilibrium, then Jeans’ theorem states that the phase space density should be a function of the integrals of the motion: total angular momentum,  $L$ , the  $z$  component of the angular momentum,  $L_z$ , and the energy,  $E$ . The total angular momentum and energy define the radius and eccentricity of an orbit. If the eccentricity distribution can be ignored, one is left with a dependence on radius. The ratio of  $L_z$  to  $L$  defines the inclination of the orbit. Thus the cloud should be describable by a function  $f(r, i)$ , which suggests that *fan-shaped* models should be used. While  $f(r, i)$  allows for the “bands” seen by IRAS, the comet trails are clearly non-equilibrium structures outside the scope of these models. Moreover, the center from which  $r$  is measured and the axis from which  $i$  is measured depend on planetary perturbations<sup>9</sup> and are both functions of  $r$ . Clearly a lot of effort will be needed to achieve the hoped for removal of the zodiacal light to an accuracy of 1% of the peak emission.

After the depletion of the liquid helium, the DIRBE JKLM channels continued to operate. The interior temperature of the Dewar appears to have stabilized at  $\approx 55$  K, which is adequate for the InSb detectors used in these bands. While the “blanked-off” noise in these channels has risen due to the increased temperature, the noise while observing the sky is dominated by the confusion noise due to the multitude of faint stars. These “warm” data have been used to provide star sightings for the attitude determination.

#### 4. DMR Observations

The Differential Microwave Radiometers (DMR) experiment on *COBE* is designed to measure small temperature differences from place to place on the sky. The DMR

consists of three separate units, one for each of the three frequencies of 31.5, 53 and 90 GHz. The field of view of each unit consists of two beams that are separated by a  $60^\circ$  angle that is bisected by the spin axis. Each beam has a  $7^\circ$  FWHM. The DMR is only sensitive to the brightness difference between these two beams. This differencing is performed by a ferrite waveguide switch that connects the receiver input to one horn and then the other at a rate of 100 Hz. The signal then goes through a mixer, an IF amplifier and a video detector. The output of the video detector is demodulated by a lock-in amplifier synchronized to the input switch. The difference signal that results is telemetered to the ground every 0.5 seconds. Each radiometer has two channels: A and B. In the case of the 31.5 GHz radiometer, the two channels use a single pair of horns in opposite senses of circular polarization. In the 53 and 90 GHz radiometers there are 4 horns, and all observe the same sense of linear polarization.

The basic problem in the DMR data analysis is to construct a map of the sky using the  $6 \times 10^7$  differences that are collected each year in each of the six channels. There are only about  $10^3$  beam areas on the sky, so the problem is highly over-determined. We have chosen to analyze the data using 6,144 pixels to cover the sky. These are approximately equal area, and arranged in a square grid of  $32 \times 32$  pixels on each of the 6 faces of a cube. Within each pixel we assume that the temperature is constant, so we are modeling the sky with a staircase function. Therefore the basic problem can be represented as a least-squares problem with  $6 \times 10^7$  equations in 6,144 variables. One way to solve this problem is to average all of the observations of each pixel. This gives the temperature of the pixel relative to its “reference ring” of pixels  $60^\circ$  away. Figure 1 shows the reference ring for pixel 4342 which contains the galactic center. Then correct the average for each pixel by the weighted mean of the temperatures in the reference ring. The correction must be iterated using the corrected temperatures until the process converges, but the convergence is slow. In practice, the DMR maps are computed by inverting the  $6144 \times 6144$  matrix of normal equations. Fortunately this matrix  $A_{ij}$  is sparse and symmetric. Thus only  $9 \times 10^5$  elements need to be kept. Figure 1 can be viewed as a map made by plotting  $A_{ij}$  at the position of the  $i^{th}$  pixel while  $j$  is fixed at  $j = 4342$ . The diagonal  $A_{ii}$  shown in Figure 2 shows the number of observations per pixel. This figure is plotted in galactic coordinates to better show the structure of the heavily covered rings  $26^\circ$  and  $34^\circ$  from the ecliptic poles. The coverage near the North ecliptic pole is reduced because the Earth limb rises above the sun shade over the North pole during the May-July eclipse season.

## 5. DMR Results

The basic DMR result is the discovery of an intrinsic anisotropy<sup>10</sup> of the microwave background, beyond the dipole anisotropy<sup>11,12</sup>. This anisotropy, when a monopole and dipole fit to  $|b| > 20^\circ$  is removed from the map, and the map is then smoothed

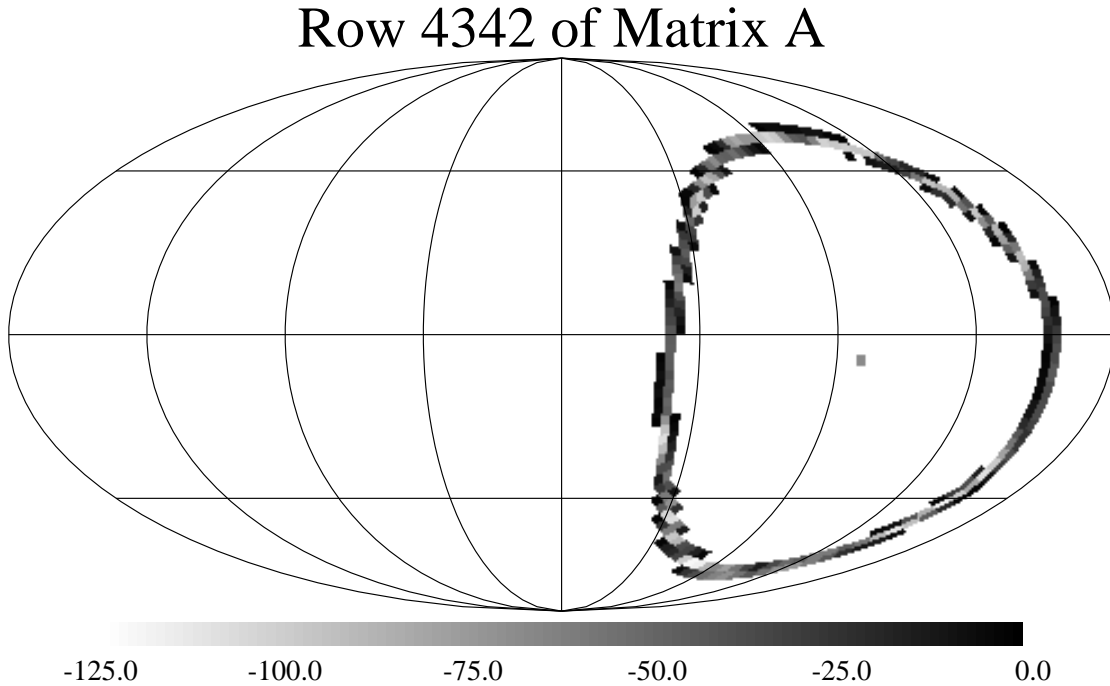


Figure 1: The column through pixel 4342 of the matrix A for the 53 GHz A channel. The central pixel contains the galactic center, and is saturated with a value of 10,599. Ecliptic coordinates are used for this plot.

to a resolution of  $\approx 10^\circ$ , is  $30 \mu\text{K}$ . The correlation function of this anisotropy is well fit by the expected correlation function for the Harrison-Zeldovich<sup>13,14,15</sup> spectrum of primordial density perturbations predicted by the inflationary scenario, and the amplitude is consistent with many models of structure formation<sup>16</sup>. Galactic emission<sup>17</sup>, systematic errors<sup>18</sup> and known extra-galactic sources<sup>19</sup> cannot explain the observed signal.

Even though the noise per pixel is much larger than the cosmic anisotropy, the detection of anisotropy has a high statistical confidence level because of the large number of pixels in the DMR maps. To illustrate this point, Figure 3 shows the unsmoothed A and B side 53 GHz maps from the initial data products, plus the smoothed difference and sum maps. Compare these to a test case with a known map, degraded to a comparable signal to noise ratio, shown in Figure 4. Clearly a pattern of some sort is starting to emerge in the smoothed sum map. Figure 5 shows the two auto-correlations and the cross-correlation that can be computed from the unsmoothed test case maps. The solid curve in this figure is the known correlation function based on the known input map. (A noiseless high resolution picture of the input map is in Figure 13.) Clearly the DMR maps show statistically

## Coverage Map for 53A Channel

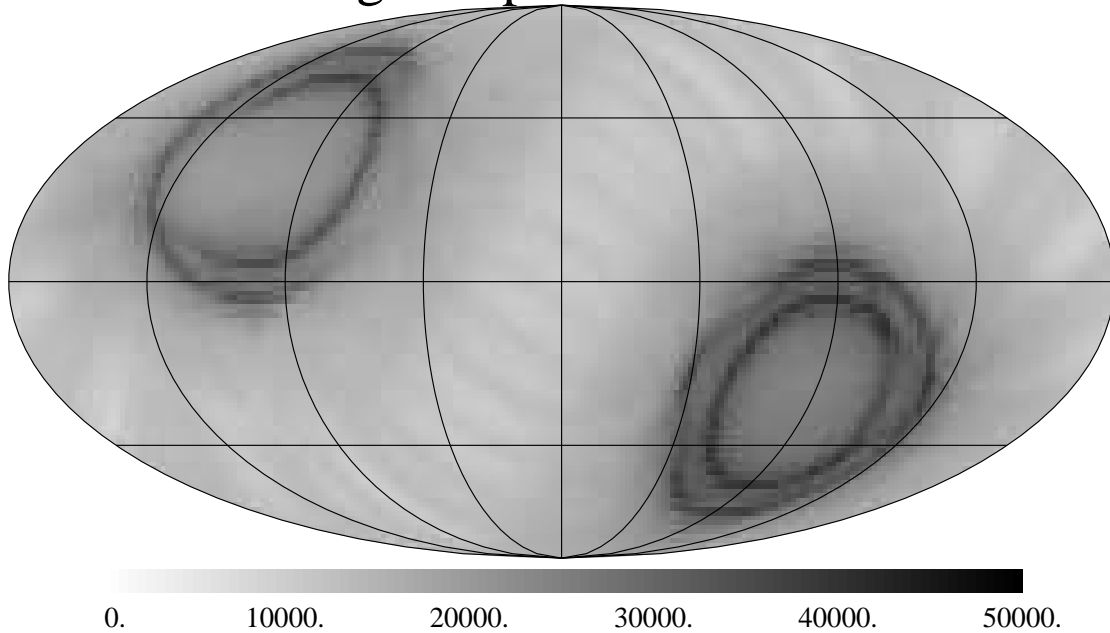


Figure 2: The diagonal of the matrix  $A$  for the 53 A channel, otherwise known as the coverage map, in galactic coordinates.

significant correlated structure. The dashed curve is the correlation function of a Harrison-Zeldovich model with equal power on all scales, smoothed to the DMR resolution, with the amplitude adjusted to match the test case. The relatively good agreement between the dashed curve and the test case correlation function shows that the good agreement between the DMR correlation function and the Harrison-Zeldovich model<sup>10</sup>, while supporting inflation, does not prove inflation.

The inflationary scenario also predicts that the temperature fluctuations should have a Gaussian distribution. This can be tested by looking at higher-order moments of the maps such as three point correlation functions, or by directly studying the probability distributions. The random measurement noise from the radiometers is still sufficient to interfere with these studies to a great extent, but a preliminary analysis finds that the Gaussian model is consistent with the observations. Figure 6 shows histograms constructed from the smoothed DMR maps. To minimize the radiometer noise, the thermodynamic  $\Delta T$ 's derived from the 53 and 90 GHz channels have been averaged together with weights of 0.6 and 0.4 respectively. The histogram of the  $(A-B)/2$  difference map is not expected to be Gaussian, because of the large variation in integration time per pixel seen in Figure 2. However, a Gaussian convolved with the  $(A-B)/2$  histogram should match the histogram of the  $(A+B)/2$  map if the sky

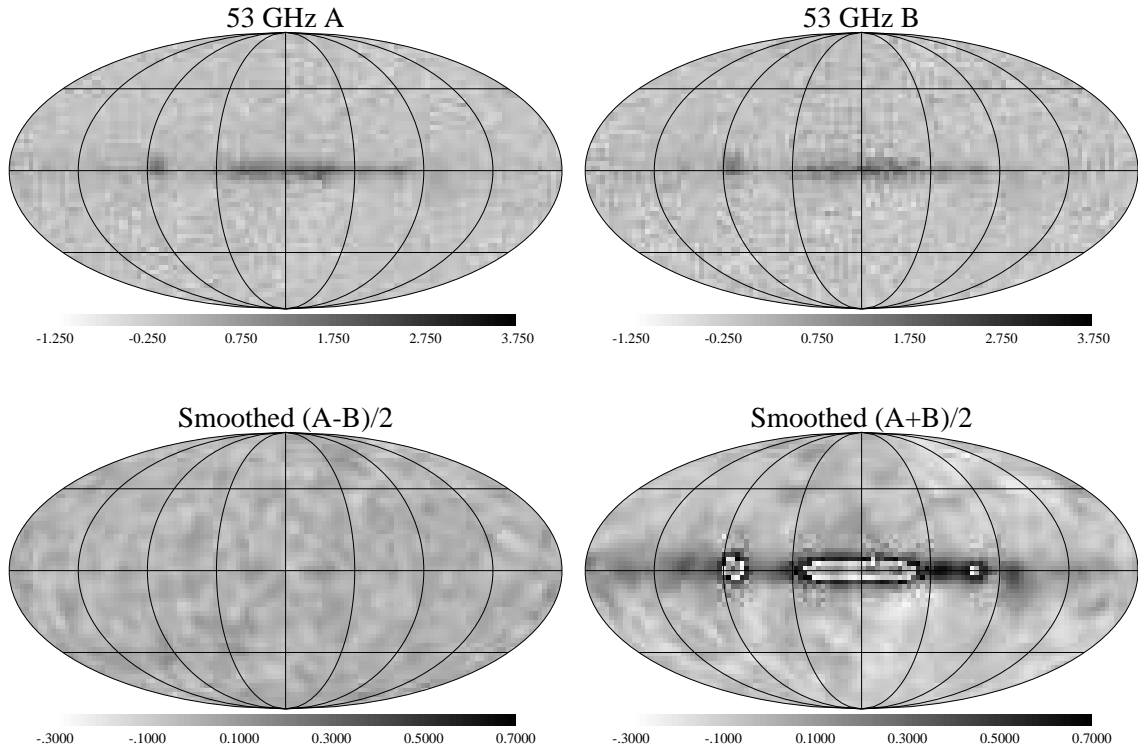


Figure 3: The unsmoothed 53 GHz A & B maps from the initial COBE data products, and the smoothed sum and difference maps.

has a Gaussian distribution. As Figure 6 shows, the “Gaussian” curve, which is this convolution, matches the observed histogram well. Detailed calculations show that models which predict non-Gaussian temperature fluctuations, such as cosmic strings<sup>20</sup> or global monopoles<sup>21</sup>, can also match the observed histogram. This convergence toward Gaussian probability distributions is caused by the  $10^\circ$  effective resolution of the smoothed maps, which averages many small patches together. Thus cosmic strings, which predict dramatically non-Gaussian behavior (sharp edges) on small scales, give almost Gaussian results after smoothing. However, some models could be rejected: Figure 7 shows the histograms from the test case maps in Figure 4. Here the non-Gaussian structure is correlated over large distances, so the smoothing does not erase it.

The ratio of the gravitational potential fluctuations seen by the DMR through the Sachs-Wolfe<sup>22</sup> effect to the gravitational potentials inferred from the bulk flows of galaxies using the POTENT method<sup>23</sup>, shows that the Harrison-Zeldovich spectrum has the correct slope to connect the DMR data at  $3 \times 10^5$  km/sec scales to the bulk flow data at 6000 km/sec scale. This comparison of the horizon-scale perturbations seen

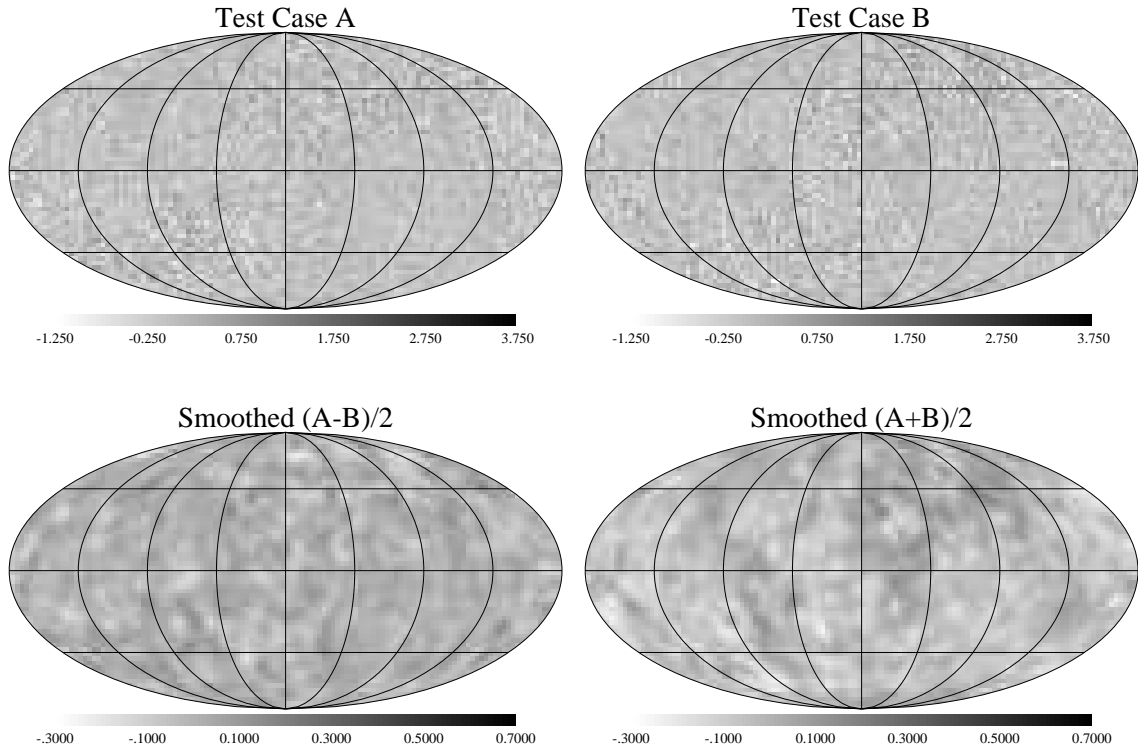


Figure 4: The unsmoothed test case A & B maps made by degrading a known pattern to the DMR resolution and signal to noise ratio, and the smoothed sum and difference maps.

by *COBE* and the “large-scale” ( $60/h$  Mpc, where  $h = H_o/(100 \text{ km s}^{-1} \text{ Mpc}^{-1})$ ) structure data gives best determination of the slope of the power spectrum of the primordial perturbations, even though it is model-dependent. *COBE* data alone cover such a small range of scales that slope determinations are uncertain.

Wright *et al.*<sup>16</sup> discussed the implications of the *COBE* DMR data for models of structure formation, and selected 4 models from a large collection<sup>24</sup> for detailed discussion: a “CDM” model, with  $H_o = 50 \text{ km s}^{-1} \text{ Mpc}^{-1}$ ,  $\Omega_{CDM} = 0.9$ , and  $\Omega_B = 0.1$ ; a mixed “CDM+HDM” model, with  $H_o = 50 \text{ km s}^{-1} \text{ Mpc}^{-1}$ ,  $\Omega_{CDM} = 0.6$ ,  $\Omega_{HDM} = 0.3$  (a 7 eV neutrino), and  $\Omega_B = 0.1$ ; an open model, with  $H_o = 100 \text{ km s}^{-1} \text{ Mpc}^{-1}$ ,  $\Omega_{CDM} = 0.18$ , and  $\Omega_B = 0.02$ ; and a vacuum dominated model, with  $H_o = 100 \text{ km s}^{-1} \text{ Mpc}^{-1}$ ,  $\Omega_{CDM} = 0.18$ ,  $\Omega_B = 0.02$ , and  $\Omega_{vac} = 0.8$ . The vacuum dominated model and especially the open model have potential perturbations now that are too small to explain the POTENT bulk flows<sup>23</sup>. Note that all of these models are normalized to the *COBE* anisotropy at large scales at  $z = 10^3$ , but in the open and vacuum-dominated models the potential perturbations go down even at the

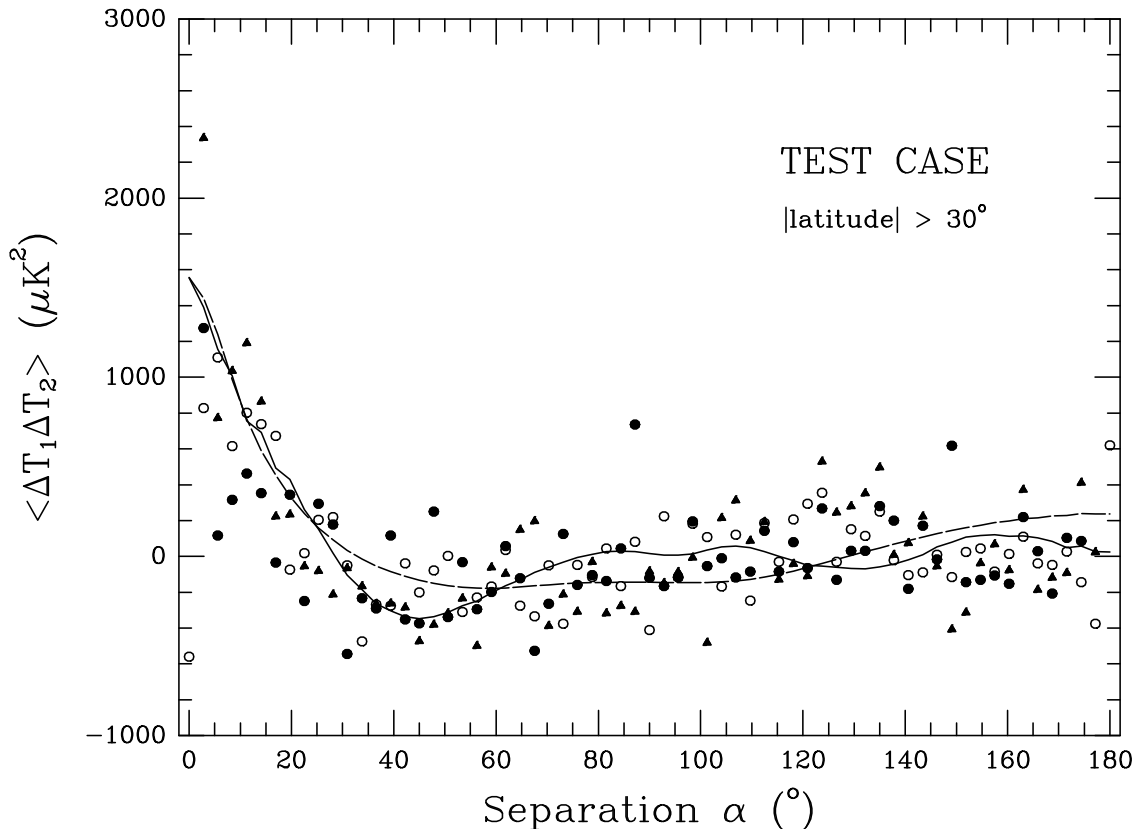


Figure 5: The auto-correlations of the test case A & B maps (solid dots), the cross-correlation (open circles), and the correlation function of the known input pattern at DMR resolution. Also shown as a dashed curve is the correlation function of an  $n = 1$  Harrison-Zeldovich model.

largest scales which are not affected by non-linearities or the transfer function. The small-scale anisotropies predicted by these models are close to the upper limits, and in the case of the  $1.5^\circ$  beam South Pole experiment<sup>25</sup> (SP) they exceed the current data. Since the DMR datum is at  $\ell_{eff} = 4$  while the SP datum is at  $\ell_{eff} = 44$ , a tilted model which replaces the Harrison-Zeldovich  $n = 1$  in  $P(k) \propto k^n$  with an  $n \approx 0.5$  would eliminate this discrepancy. But such a low  $n$  would destroy the agreement between the bulk flow velocities and the COBE  $\langle Q_{RMS}^2 \rangle^{0.5}$ . In fact the POTENT bulk flows are inconsistent with the SP  $\Delta T$  data<sup>26</sup>, while other bulk flow determinations are even larger<sup>27</sup>.

Wright<sup>28</sup> has computed the power spectrum of the DMR maps using the Hauser-Peebles method to allow for incomplete sky coverage caused by masking out the galactic plane region. Figure 8 shows the power in each multipole normalized to a pure  $n = 1$  (Harrison-Zeldovich) power law with  $\langle Q_{RMS}^2 \rangle^{0.5} = 17 \mu K$ . Also shown

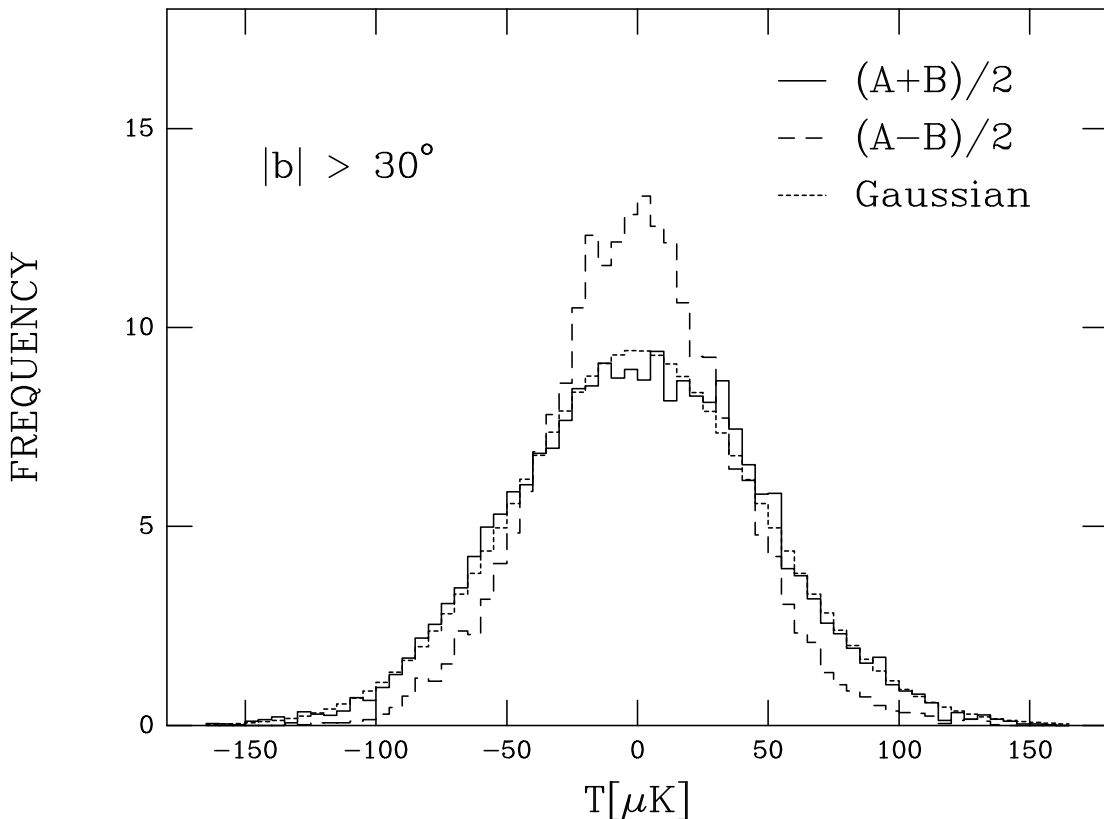


Figure 6: The histogram of the smoothed 1 year 53+90 GHz (A-B)/2 map, its convolution by a Gaussian, which matches the observed histogram of the (A+B)/2 map.

are results from various small and medium scale  $\Delta T$  experiments. For perturbations at scales smaller than the horizon at the end of radiation dominance, dynamical effects boost the expected anisotropy. At very small scales, the finite thickness of the recombination surface filters out most of the anisotropy. The models shown in Figure 8 are an  $n = 0.85$  tilted CDM model<sup>29</sup> (lower curve, with  $H_0 = 50 \text{ km s}^{-1} \text{ Mpc}^{-1}$  and  $\Omega_B h^2 = 0.0125$ ), and the same model with the  $n = 0.96$  expected from chaotic  $\phi^4$  inflation. The POTENT bulk flow, if translated into a  $\Delta T_\ell^2$  in Figure 8, would correspond to a point on the higher model curve at  $\ell \approx 100$ . The Lauer & Postman<sup>27</sup> bulk flow would correspond to a  $\Delta T_\ell^2$  that is  $\approx 40$  times higher than the higher model at  $\ell \approx 40$ . Clearly the tilt of the primordial power spectrum cannot be determined without much better measurements of small scale  $\Delta T$  and bulk flow velocities. Note that the RING experiment<sup>38</sup> is known to be contaminated by discrete sources, but the power spectrum of uncorrelated point sources is  $\propto \ell^2$  in Figure 8, so this population has a negligible effect on the data at lower  $\ell$ 's for sources which emit a spectrum similar to the spectrum of the Milky Way. When comparing these data to the *COBE*

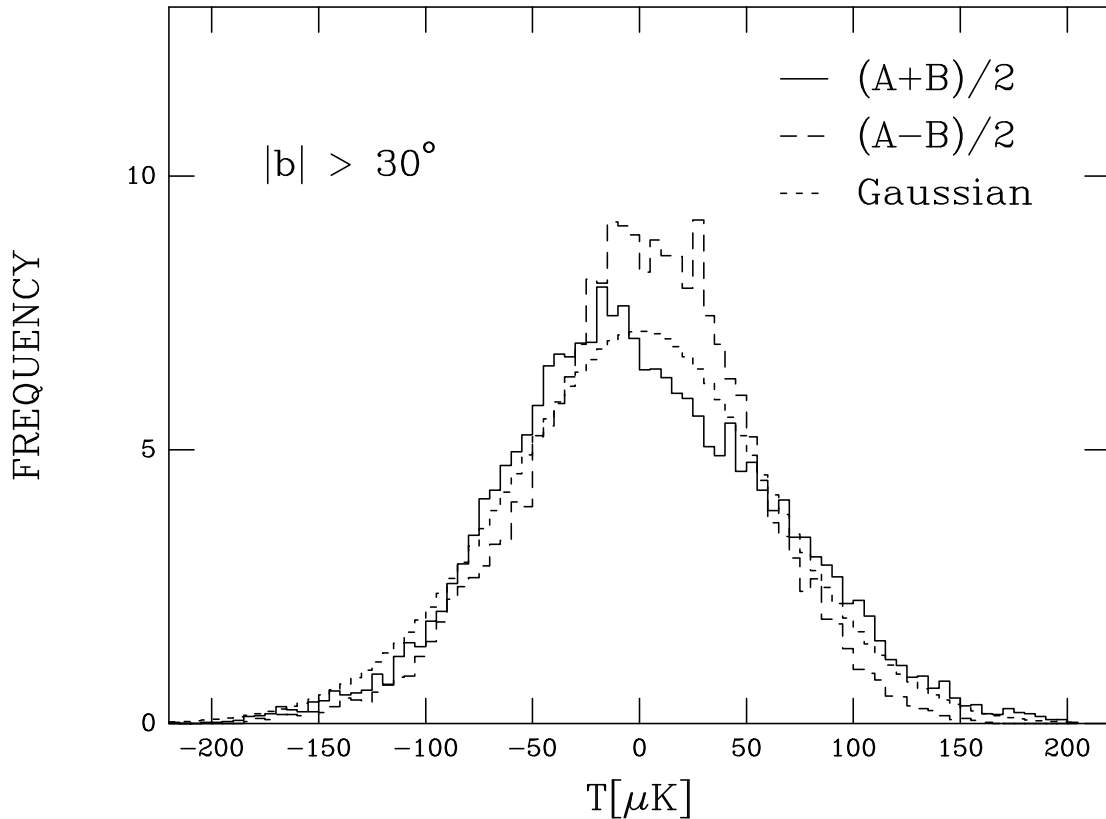


Figure 7: The histogram of the smoothed  $(A-B)/2$  test case map, and its convolution by a Gaussian, which fails to match the observed histogram of the  $(A+B)/2$  map.

DMR data the corrections for the galactic plane cut and the non-Gaussian shape of the DMR beam should be used<sup>30</sup>.

## 6. FIRAS Measurements

The Far InfraRed Absolute Spectrophotometer instrument on *COBE* is a polarizing Michelson<sup>31</sup> interferometer. The optical layout is symmetrical, and it has two inputs and two outputs. If the two inputs are denoted SKY and ICAL, then the two outputs, which are denoted LEFT and RIGHT, are given symbolically as

$$\text{LEFT} = \text{SKY} - \text{ICAL} \quad (1)$$

$$\text{RIGHT} = \text{ICAL} - \text{SKY} \quad (2)$$

The FIRAS has achieved its incredible sensitivity to small deviations from a blackbody spectrum by connecting the ICAL input to an internal calibrator, a reference

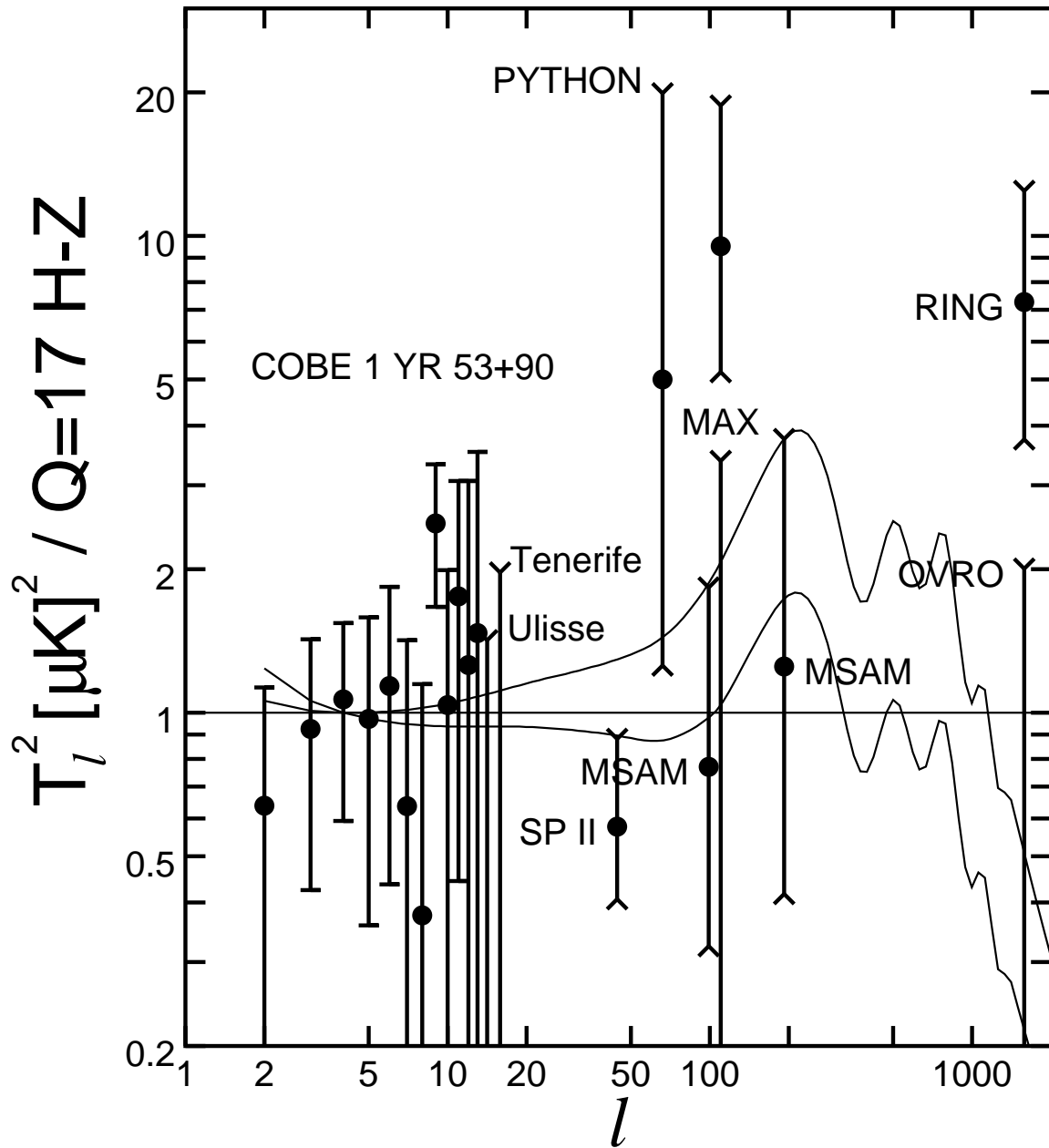


Figure 8: The angular power spectrum of the CMBR, normalized to an  $\langle Q_{RMS}^2 \rangle^{0.5} = 17 \mu\text{K}$  Harrison-Zeldovich model. Data from  $\ell = 2..13$  are from COBE. Other data and upper limits are from left to right: Ulisse<sup>32</sup>, Tenerife<sup>33</sup>, SP II<sup>25</sup>, PYTHON<sup>34</sup>, MSAM<sup>35</sup>, two points from MAX<sup>36,37</sup>, MSAM again, RING<sup>38</sup> and OVRO<sup>39</sup>.

blackbody that can be set to a temperature close to the temperature  $T_o$  of the sky. Thus this “absolute” spectrophotometer is so successful because it is differential. In addition, each output is further divided by a dichroic beamsplitter into a low frequency channel ( $2\text{-}21\text{ cm}^{-1}$ ) and a high frequency channel ( $23\text{-}95\text{ cm}^{-1}$ ). Thus there are four overall outputs. These are labeled LL (left low) through RH (right high).

Each output has a large composite bolometer that senses the output power by absorbing the radiation, converting this power into heat, and then detecting the temperature rise of a substrate using a small and sensitive silicon resistance thermometer. In order to minimize the specific heat of the bolometer, which maximizes the temperature rise for a given input power, the substrate is made of the material with the highest known Debye temperature: diamond. Diamond is transparent to millimeter waves, however, so an absorbing layer is needed. Traditionally a layer of bismuth has been used as the absorber on composite bolometers, but the FIRAS detectors use a thin layer of gold alloyed with chromium. The absorbing layer needs to have a surface impedance about one-half of the  $377\text{ Ohms}/\square$  impedance of free space in order to absorb efficiently, and this surface impedance can be obtained with a much thinner layer of gold rather than bismuth. Again, this serves to minimize the specific heat of the detector. In order to detect the longest waves observed by FIRAS, the diameter of the octagonal diamond substrate is large: about 8 mm. Each detector sits behind a compound parabolic concentrator, or Winston cone, which provides a full  $\pi$  steradians in the incoming beam. As a result, the FIRAS instrument has a large étendue of  $1.5\text{ cm}^2\text{ sr}$ .

Since the FIRAS is a Michelson interferometer, the spectral data are obtained in the form of interferograms. Thus the LEFT output is approximately

$$I_L(x) = \int_0^\infty \cos(2\pi\nu x)G(\nu) \left( I_\nu + \sum_i \epsilon_i(\nu)B_\nu(T_i) + U_\nu \right) d\nu \quad (3)$$

The index  $i$  above runs over all the components in the FIRAS that had thermometers to measure  $T_i$ . These include the ICAL, the reference horn that connects to the ICAL, the sky horn, the bolometer housing, the optical structure of the FIRAS, and the dihedral mirrors that move to provide the variation in path length difference  $x$ . The  $\epsilon_i$ 's are the effective emissivities of the various components. The ICAL itself has  $\epsilon \approx -1$ , while the sky and reference horns have  $\epsilon$ 's of  $\pm$  a few percent in the low frequency channels. The offset term  $U_\nu$  was observed during flight to be approximately  $10^{-5} \exp(-t/\tau)B_\nu(T_U)$  with a time constant  $\tau$  of two months and a temperature  $T_U \approx 15\text{ K}$ . The SKY input  $I_\nu$  above can be either the sky or an external calibrator. The XCAL is a movable re-entrant absorber that can be inserted at the top of the sky horn. The combination of sky horn plus XCAL forms a cavity with an absorbtivity known to be  $> 0.9999$  from measurements, and believed to be  $\gtrsim 0.99999$  from calculations. With the XCAL inserted during periodic calibration runs, the SKY input is known to be  $B_\nu(T_X)$ . By varying  $T_X$  and the other  $T_i$ 's, the calibration

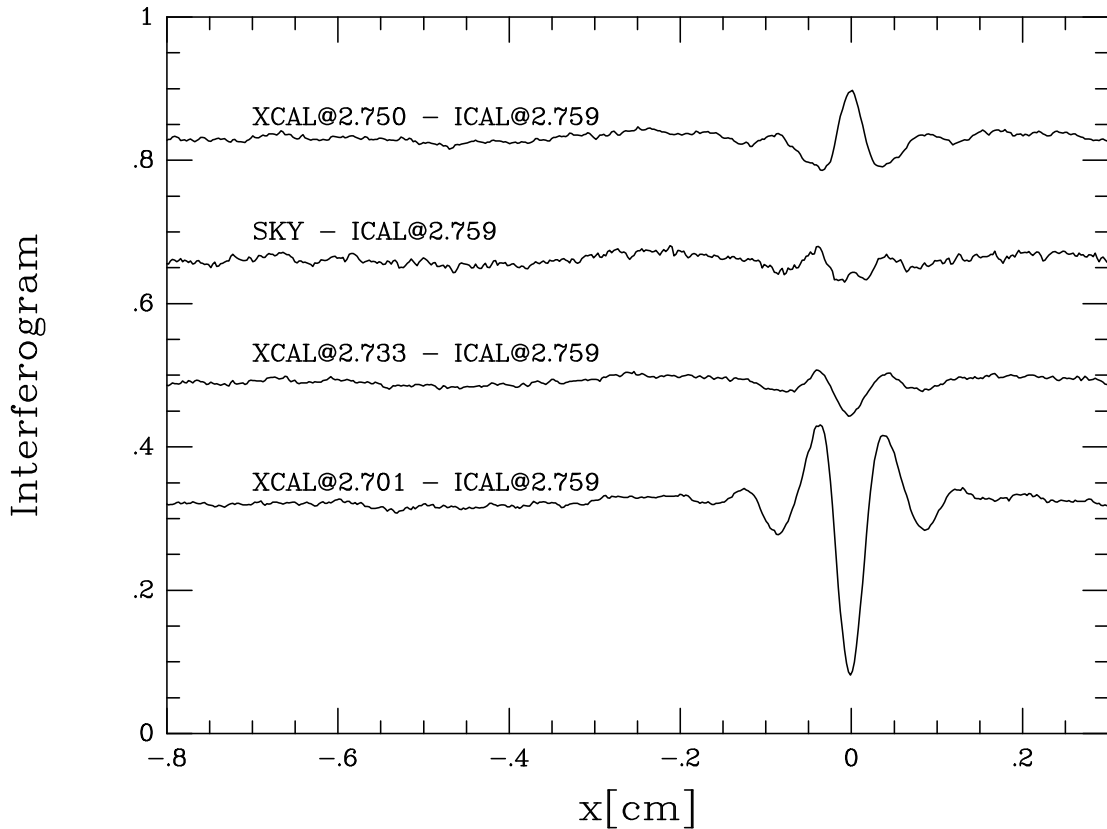


Figure 9: Co-added FIRAS interferograms from the Left Low channel taken during flight with the ICAL at 2.759 K while looking at the sky or the XCAL at 2.701, 2.733 or 2.750 K.

coefficients have been determined<sup>40</sup>. Figure 9 shows the interferograms from flight used to determine the preliminary FIRAS spectrum<sup>41</sup>.

Once the calibration coefficients are known, the sky data can be analyzed to determine  $I_\nu(l, b)$  the intensity of the sky as a function of frequency, galactic longitude and galactic latitude. This is a “data cube”. The data from each direction on the sky can be written as a combination of cosmic plus galactic signals:

$$\begin{aligned}
 I_\nu(l, b) &= e^{-\tau_\nu(l, b, \infty)} (B_\nu(T_\circ + \Delta T(l, b)) + \Delta I_\nu) \\
 &+ \int e^{-\tau_\nu(l, b, s)} j_\nu(l, b, s) ds
 \end{aligned}
 \tag{4}$$

where  $\tau_\nu(l, b, s)$  is the optical depth between the Solar system and the point at distance  $s$  in the direction  $(l, b)$  at frequency  $\nu$ ,  $\Delta I_\nu$  is an isotropic cosmic distortion, and  $\Delta T(l, b)$  is the variation of the background temperature around its mean value  $T_\circ$ . This equation can be simplified because the optical depth of the galactic dust emission

is always small in the millimeter and sub-millimeter bands covered by FIRAS.

$$I_\nu(l, b) \approx B_\nu(T_\circ + \Delta T(l, b)) + \Delta I_\nu + \int j_\nu(l, b, s) ds \quad (5)$$

Even in the optically thin limit, some restrictive assumptions about the galactic emissivity  $j_\nu$  are needed, since the galactic intensity  $\int j_\nu(l, b, s) ds$  is a function of three variables, just like the observed data. The simplest reasonable model<sup>42</sup> for the galactic emission is

$$\int j_\nu(l, b, s) ds = G(l, b)g(\nu). \quad (6)$$

This model assumes that the shape of the galactic spectrum is independent of direction on the sky. It is reasonably successful except that the galactic center region is clearly hotter than the rest of the galaxy. The application of this model proceeds in two steps. The first step assumes that the cosmic distortions vanish, and that an approximation  $g_\circ(\nu)$  to the galactic spectrum is known. A least squares fit over the spectrum in each pixel then gives the maps  $\Delta T(l, b)$  and  $G(l, b)$ . The high frequency channel of FIRAS is used to derive  $G(l, b)$  because the galactic emission is strongest there. An alternative way to derive  $G(l, b)$  is to smooth the DIRBE map at 240  $\mu\text{m}$  to the FIRAS  $7^\circ$  beam. This DIRBE method has been used in the latest FIRAS spectral results<sup>43,44,45</sup>. The second step in the galactic fitting then derives spectra associated with the main components of the millimeter wave sky: the isotropic cosmic background, the dipole anisotropy, and the galactic emission. This fit is done by fitting all the pixels (except for the galactic center region with  $|b| < 20$  and  $|l| < 40$ ) at each frequency to the form

$$I_\nu(l, b) = I_\circ(\nu) + D(\nu) \cos \theta + G(l, b)g(\nu). \quad (7)$$

The spectra of the anisotropic components derived from this fit applied to the entire mission data set are shown in Figures 10 and 11. Figure 11 shows the residual<sup>44</sup> after the predicted dipole spectrum  $\Delta T \partial B_\nu / \partial T$  evaluated at  $T_\circ$  is subtracted from  $D(\nu)$ .

But the FIRAS calibration model is so complicated and the cosmic distortions, if any, are so small, that there are still systematic uncertainties that limit the accuracy of the isotropic spectrum  $I_\circ(\nu)$  derived from the whole FIRAS data set. Therefore the best estimate of  $I_\circ(\nu)$  comes from the last six weeks of the mission, when a modified observing sequence consisting of 3.5 days of observing the sky with the ICAL set to null out the cosmic spectrum, followed by 3.5 days of observing the XCAL with its temperature set to match the sky temperature  $T_\circ$ . Six cycles of this alternation between sky and XCAL were obtained before the helium ran out. By processing both the sky data and the XCAL data through the same calibration model, and then subtracting the two spectra, almost all of the systematic errors cancel out. The residual in the high galactic latitude sky is then modeled as

$$I_\nu(\text{sky}, |b| > b_c) - I_\nu(\text{XCAL}) = \Delta I_\nu + \delta T \frac{\partial B_\nu}{\partial T} + Gg(\nu). \quad (8)$$

The result of a least squares fit to minimize  $\Delta I_\nu$  by adjusting  $\delta T$  and  $G$  is shown in Figure 10. Since all of the data taken during the last six weeks of the mission were taken in a single scan mode, the mechanical resonance frequency of the mirror carriage occurs at a fixed spectral frequency, leading to the large error bar on the point at  $11 \text{ cm}^{-1}$ . The data points show the residuals while the curves show the “uninteresting” models  $\partial B_\nu/\partial T$  and  $g(\nu)$ , and the “interesting”  $y$  and  $\mu$  models. It is important to remember that any cosmic distortion with a spectral shape that matches one of the uninteresting curves will be hidden in this fit. The maximum residual between  $2$  and  $20 \text{ cm}^{-1}$  is 1 part in 3000 of the peak of the blackbody, and the weighted RMS residual is 1 part in  $10^4$  of the peak of the blackbody. While these residuals are small, they are nonetheless more than twice the residuals that one would expect from detector noise alone. The error bars in Figure 10 have been inflated by a constant factor to give  $\chi^2 = 32$  for the 32 degrees of freedom in the fit. Limits on cosmological distortions can now be set by adding terms to the above fit, finding the best fit value with minimum  $\chi^2$ , and then finding the endpoints of the 95% confidence interval where  $\chi^2 = \chi_{min}^2 + 4$ . As an example of such a fit, suppose that the sky in fact was a gray-body with an emissivity  $\epsilon = 1 + e$ , where  $e$  is a small parameter. Since the XCAL is a good blackbody, this model predicts a residual of the form  $eB_\nu(T_\circ)$ . Because  $B_\nu(T_\circ)$  peaks at a lower frequency than  $\partial B_\nu/\partial T$ , this model is sufficiently different from the “uninteresting” models and a tight limit on  $e$  can be set:  $|e| < 0.00041$  (95% confidence). The result of fits for the usual cosmological suspects are  $|y| < 2.5 \times 10^{-5}$  and  $|\mu| < 3.3 \times 10^{-4}$  with 95% confidence.

The absolute temperature of the cosmic background,  $T_\circ$ , can be determined two ways using FIRAS. The first way is to use the readings of the germanium resistance thermometers in the XCAL when the XCAL temperature is set to match the sky. This gives  $T_\circ = 2.730 \text{ K}$ . The second way is to measure the frequency of the peak of  $\partial B_\nu/\partial T$  by varying  $T_X$  a small amount around the temperature which matches the sky, and then apply the Wien displacement law to convert this frequency into a temperature. This calculation is done automatically by the calibration software, and it gives a value of  $2.722 \text{ K}$  for  $T_\circ$ . Three additional determinations of  $T_\circ$  depend on the dipole anisotropy. For either FIRAS or DMR, the spectrum of the dipole anisotropy can be fit to the form

$$D(\nu) = \frac{T_\circ v}{c} \frac{\partial B_\nu(T_\circ)}{\partial T} \quad (9)$$

Since the velocity of the solar system with respect to the CMB is not known *a priori*, only the shape and not the amplitude of the dipole spectrum can be used to determine  $T_\circ$ . For FIRAS, this analysis gives  $T_\circ = 2.714 \pm 0.022 \text{ K}^{44}$ , while for DMR it gives  $T_\circ = 2.76 \pm 0.18 \text{ K}^{12}$ . The DMR data analysis keeps track of the changes in the dipole caused by the variation of the Earth’s velocity around the Sun during the year. In this case the velocity  $v$  is known, so  $T_\circ$  can be determined from the amplitude of the change in the dipole, giving  $T_\circ = 2.75 \pm 0.05 \text{ K}^{12}$ . The final adopted value is  $2.726 \pm 0.010 \text{ K}^{43}$  (95% confidence), which just splits the difference between the two

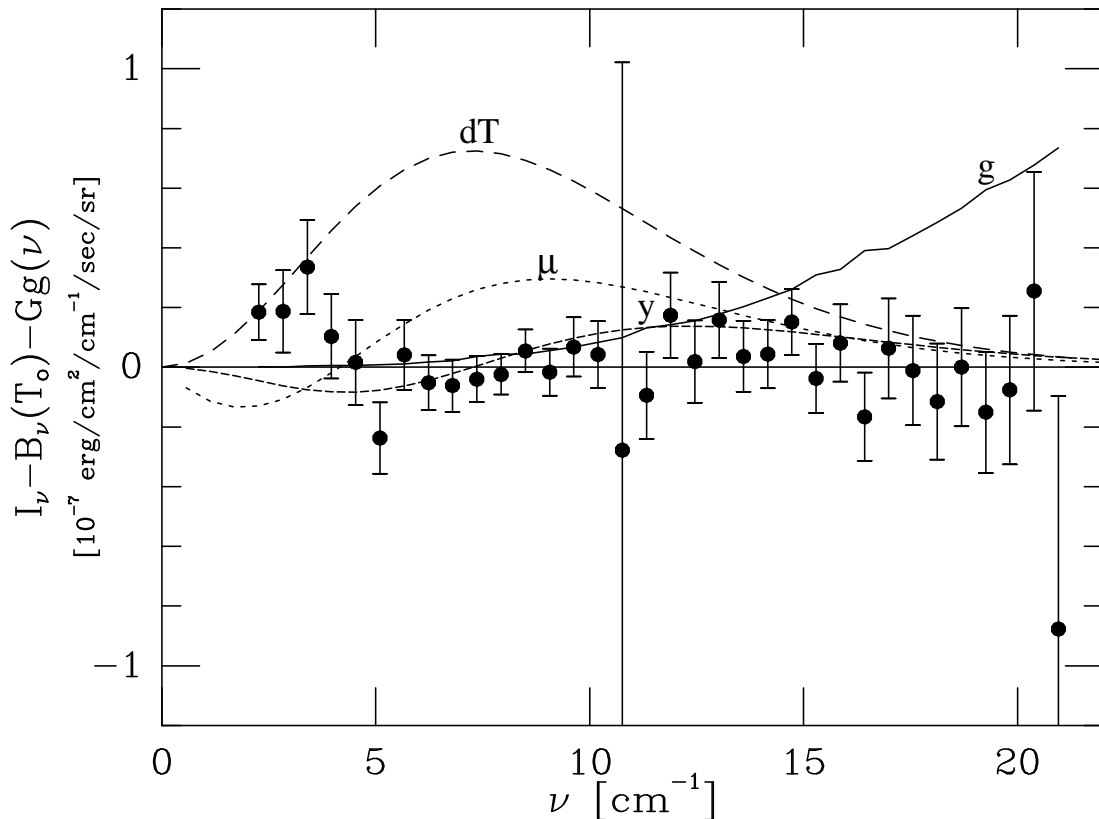


Figure 10: FIRAS residuals (points) after fitting for a blackbody and galactic emission, with an 0.5 mK  $\Delta T$ , a  $\Delta(\text{csc } |b|) = 0.25$  galaxy curve,  $y = 2.5 \times 10^{-5}$ , and  $\mu = 3.3 \times 10^{-4}$  shown for comparison. Full-scale is 0.1% of the peak of the CMB.

methods based on the FIRAS spectra. The dipole-based determinations of  $T_0$  are less precise but provide a useful confirmation of the spectral data.

## 7. FIRAS Interpretation

When interpreting the implications of the FIRAS spectrum on effects that could distort the microwave background, it is important to remember some basic order-of-magnitude facts. Theoretical analyses of light element abundances gives limits on the current density of baryons through models of Big Bang NucleoSynthesis (BBNS). The ratio of baryons to photons<sup>46</sup> is  $\eta = (3.5 \pm 0.7) \times 10^{-10}$ , while another determination<sup>47</sup> gives  $\eta = (3.95 \pm 0.25) \times 10^{-10}$ . As a result, the effect of Lyman  $\alpha$  photons from recombination is negligible, simply because there are so few hydrogen atoms per photon. Since the number density of photons is well determined by the FIRAS

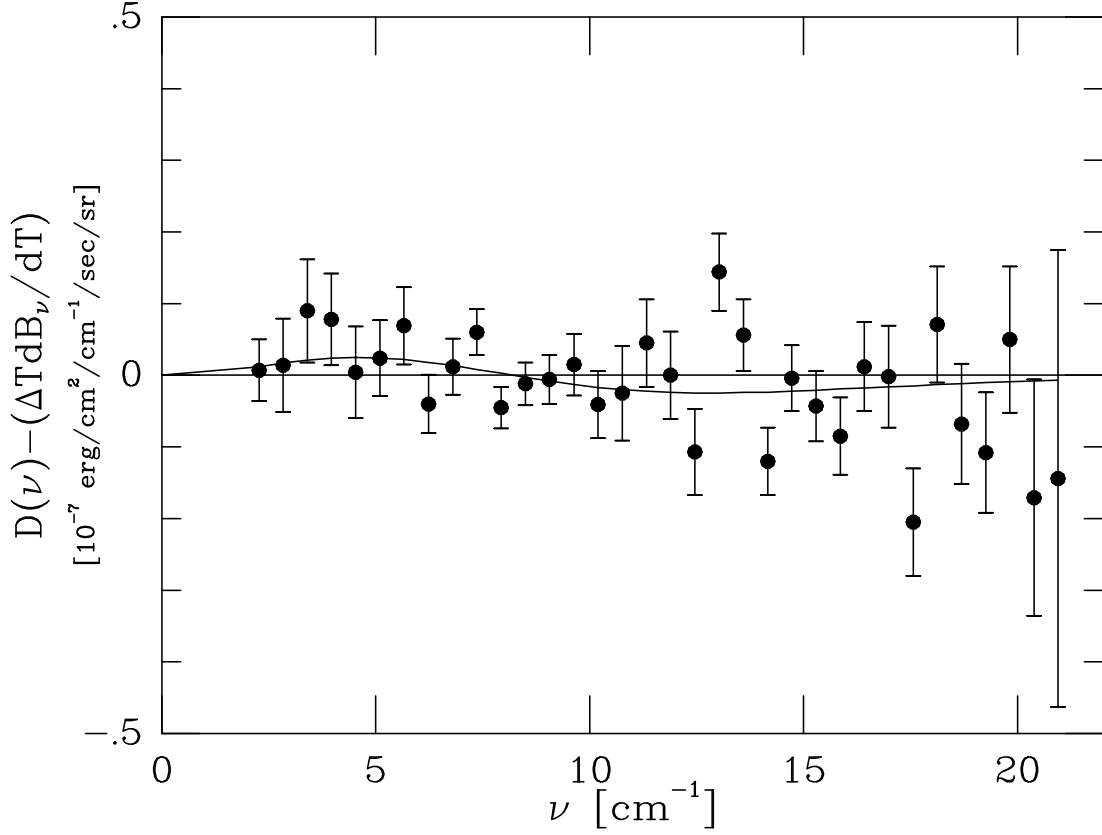


Figure 11: FIRAS Dipole spectrum residuals from an amplitude of 3.343 mK applied to  $T_o = 2.726$  K (points). Full-scale is 0.04% of the peak of the CMB. The curve shows the best fit dipole color temperature of 2.714 K with an amplitude of 3.379 mK.

spectrum

$$N = 8\pi\zeta(3)\Gamma(3) \left(\frac{kT_o}{hc}\right)^3 = 410 \pm 5 \text{ cm}^{-3} \quad (10)$$

the baryon density is well determined:  $1.62 \times 10^{-7} \text{ cm}^{-3}$ . This gives  $\Omega_B h^2 = 0.0144$ . Not all of these baryons are protons, however. For a primordial helium abundance of 23.5% by mass, one has 13 protons and 1  $\alpha$  particle in 17 baryons. This gives an electron density of  $n_{e,o} = 1.43 \times 10^{-7} \text{ cm}^{-3}$ . For a fully ionized Universe, the optical depth for electron scattering over a path length equal to the Hubble radius  $c/H_o$  is  $0.00088/h$ .

The expansion of the Universe  $H$  varies with time and redshift in a way that depends on ratios of the current matter, radiation and vacuum densities to the critical

density  $\rho_c = 3H^2/8\pi G$ . Let these ratios be  $\Omega_m$ ,  $\Omega_r$ , and  $\Omega_v$ . Then

$$H(z) = (1+z)H_0 \sqrt{(1-\Omega_m-\Omega_r-\Omega_v) + \Omega_m(1+z) + \Omega_r(1+z)^2 + \Omega_v(1+z)^{-2}} \quad (11)$$

This equation is not exact for massive neutrinos which shift from being part of  $\Omega_m$  into part of  $\Omega_r$  as  $z$  increases. The value of  $\Omega_r h^2 = (4.16 \pm 0.06) \times 10^{-5}$  is fairly well-determined for the case of three massless neutrinos. Thus if  $\Omega_m \approx 1$  now, the Universe becomes radiation dominated for  $z > z_{eq} = 2.4h^2 \times 10^4$  when the background temperature was  $kT_{eq} = 5.65h^2$  eV. In the radiation dominated epoch,  $H = 0.645(1+z)^2$  km/sec/Mpc or  $H = 2.09(1+z)^2 \times 10^{-20}$  s $^{-1}$ .

For early epochs when the Universe was ionized, electron scattering is the dominant mechanism for transferring energy between the radiation field and the matter. As long as the electron temperature is less than about  $10^8$  K, the effect of electron scattering on the spectrum can be calculated using the Kompaneets equation<sup>48</sup>:

$$\frac{\partial n}{\partial y} = x^{-2} \frac{\partial}{\partial x} \left[ x^4 \left( n + n^2 + \frac{\partial n}{\partial x} \right) \right] \quad (12)$$

where  $n$  is the number of photons per mode ( $n = 1/(e^x - 1)$  for a blackbody),  $x = h\nu/kT_e$ , and the Kompaneets  $y$  is defined by

$$dy = \frac{kT_e}{m_e c^2} n_e \sigma_T c dt. \quad (13)$$

Thus  $y$  is the electron scattering optical depth times the electron temperature in units of the electron rest mass. Note that the electrons are assumed to follow a Maxwellian distribution, but that the photon spectrum is completely arbitrary.

Since the Kompaneets equation is describing electron scattering, which preserves the number of photons, one finds that the  $y$  derivative of the photon density  $N$  vanishes:

$$\begin{aligned} \frac{\partial N}{\partial y} &\propto \int x^2 \frac{\partial n}{\partial y} dx \\ &= \int \frac{\partial}{\partial x} \left[ x^4 \left( n + n^2 + \frac{\partial n}{\partial x} \right) \right] dx \\ &= 0 \end{aligned} \quad (14)$$

The stationary solutions of the equation  $\partial n/\partial y = 0$  are the photon distributions in thermal equilibrium with the electrons. Since photons are conserved, the photon number density does not have to agree with the photon number density in a blackbody at the electron temperature. Thus a more general Bose-Einstein thermal distribution is allowed:  $n = 1/(\exp(x + \mu) - 1)$ . This gives  $\partial n/\partial y = 0$  for all  $\mu$ . Since the

Bose-Einstein spectrum is a stationary point of the Kompaneets equation, it is the expected form for distortions produced at epochs when

$$(1+z)\frac{\partial y}{\partial z} = \sigma_T n_{e,\circ} \frac{kT_\circ}{m_e c^2} \frac{c}{H} (1+z)^4 > 1 \quad (15)$$

For the  $\Omega_B h^2$  given by BBNS, this redshift  $z_y$  where this inequality is crossed is well within the radiation dominated era, with a value  $z_y = 10^{5.1}/\sqrt{70\Omega_B h^2}$ .

There is a simple solution to the Kompaneets equation with non-zero  $\partial n/\partial y$  which gives the Sunyaev-Zeldovich<sup>49</sup> or  $y$  spectral distortion. This simple case occurs when the initial photon field is a blackbody with a temperature  $T_\gamma$  which is below the electron temperature. Letting  $f = T_e/T_\gamma$ , we find that the initial photon field is given by  $n = 1/(\exp(fx) - 1)$ . Therefore

$$\left( n + n^2 + \frac{\partial n}{\partial x} \right) = \frac{(1-f)\exp(fx)}{(\exp(fx) - 1)^2} = (1-f^{-1})\frac{\partial n}{\partial x}. \quad (16)$$

Thus the distortion has a Sunyaev-Zeldovich shape but is reduced in magnitude by a factor  $(1 - T_\gamma/T_e)$ . Defining the “distorting”  $y$  as

$$dy_D = \frac{k(T_e - T_\gamma)}{m_e c^2} n_e \sigma_T c dt \quad (17)$$

we find that the final spectrum is given by a frequency-dependent temperature given by

$$T_\nu = T_\circ \left[ 1 + y_D \left( \frac{x(e^x + 1)}{e^x - 1} - 4 \right) + \dots \right]. \quad (18)$$

where  $x = h\nu/kT_\circ$ . The FIRAS spectrum in Figure 10 shows that  $|y_D| < 2.5 \times 10^{-5}$ .

The energy density transferred from the hotter electrons to the cooler photons in the  $y$  distortion is easily computed. The energy density is given by  $U \propto \int x^3 n dx$  so

$$\frac{\partial U}{\partial y_D} = \int x \frac{\partial}{\partial x} \left( x^4 \frac{\partial n}{\partial x} \right) dx \quad (19)$$

which when integrated by parts twice gives

$$\begin{aligned} \frac{\partial U}{\partial y_D} &= - \int \left( x^4 \frac{\partial n}{\partial x} \right) dx \\ &= 4 \int x^3 n dx = 4U. \end{aligned} \quad (20)$$

Thus the limit on  $y_D$  gives a corresponding limit on energy transfer:  $\Delta U/U < 10^{-4}$ . Any energy which is transferred into the electrons at redshifts  $z > 7$  where the

Compton cooling time is less than the Hubble time will be transferred into the photon field and produce a  $y$  distortion. Since there are  $10^9$  times more photons than any other particles except for the neutrinos, the specific heat of the photon gas is overwhelmingly dominant, and the electrons rapidly cool (in a Compton cooling time) back into equilibrium with the photons. The energy gained by the photons is  $\Delta U = 4yaT_\gamma^4$  which must be equal to the energy lost by the electrons and ions:  $1.5(n_e + n_i)k\Delta T_e$ . Since  $y = \sigma_T n_e (kT_e/m_e c^2) c \Delta t$  we find the Compton cooling time

$$t_C = \frac{1.5(1 + n_i/n_e)m_e c^2}{4\sigma_T c U_{rad}} = \frac{7.4 \times 10^{19} \text{ sec}}{(1 + z)^4} \quad (21)$$

for an ion to electron ratio of 14/15. This becomes equal to the Hubble time  $(3.08568 \times 10^{17} \text{ sec})/(h(1 + z)^{1.5})$  at  $(1 + z) = 9h^{0.4}$ . Figure 12 shows the maximum allowed temperature<sup>45</sup> for an intergalactic medium heated impulsively as a function of the heating redshift. After being heated, the IGM cools by adiabatic expansion and Compton cooling. The 3 models shown in Figure 12 are an open model with  $H_o = 100 \text{ km s}^{-1} \text{ Mpc}^{-1}$ ,  $\Omega_B h^2 = 0.0125$ , and  $\Omega = 0.2$ ; a flat model with  $H_o = 50$ ,  $\Omega = 1$  and the same  $\Omega_B$ ; and a ‘‘BARYONIC’’ model with  $H_o = 50$  and  $\Omega = \Omega_B = 0.2$  which has four times more baryons than BBNS models predict. For this increased value of the baryon abundance, the allowed  $kT_{max}$  is considerably less than the 1 keV suggested by the 300 km/sec velocity dispersion in galaxies.

At redshifts  $z > z_y = 10^5$ , there will be enough electron scattering to force the photons into a thermal distribution with a  $\mu$  distortion instead of a  $y$  distortion. However, the normal form for writing a  $\mu$  distortion does not preserve the photon number density. Thus we should combine the  $\mu$  distortion with a temperature change to give an effect that preserves photon number. The photon number density change with  $\mu$  is given by

$$\begin{aligned} N &\propto \int \frac{x^2 dx}{\exp(x + \mu) - 1} \\ &= \sum_{k=1}^{\infty} e^{-k\mu} \int x^2 e^{-kx} dx \\ &= 2 \sum_{k=1}^{\infty} \frac{e^{-k\mu}}{k^3} \\ &= 2(\zeta(3) - \mu\zeta(2) + \dots). \end{aligned} \quad (22)$$

A similar calculation for the energy density shows that

$$U \propto 6(\zeta(4) - \mu\zeta(3) + \dots). \quad (23)$$

In order to maintain  $N = \text{const}$ , the temperature of the photon field changes by an amount  $\Delta T/T = \mu\zeta(2)/(3\zeta(3))$ . Therefore, the energy density change at constant  $N$

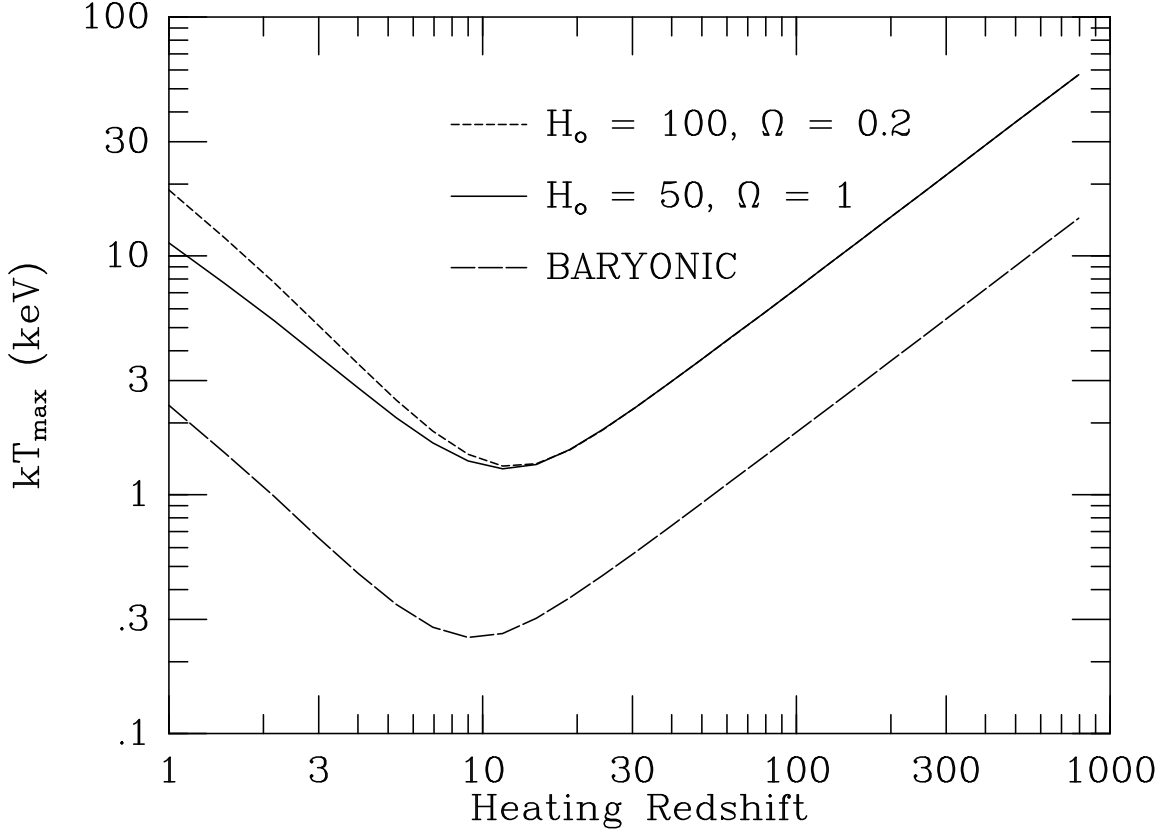


Figure 12: The maximum allowed temperature for an IGM as a function of the heating redshift for two models with the BBNS baryon abundance ( $\Omega_B h^2 = 0.0125$ ) and one model with 4 times more baryons ( $H_o = 50, \Omega = \Omega_B = 0.2$ ).

is

$$\frac{\Delta U}{U} = \left( \frac{4\zeta(2)}{3\zeta(3)} - \frac{\zeta(3)}{\zeta(4)} \right) \mu = 0.714\mu. \quad (24)$$

Thus the FIRAS limit  $|\mu| < 3.3 \times 10^{-4}$  implies  $\Delta U/U < 2.4 \times 10^{-4}$ . The “improved” form of the  $\mu$  distortion, with a  $\Delta T$  added to keep  $N$  constant, can be given as a frequency dependent brightness temperature:

$$T_\nu = T_o \left( 1 + \mu \left[ \frac{\zeta(2)}{3\zeta(3)} - x^{-1} \right] + \dots \right). \quad (25)$$

In this form it is clear that a  $\mu$  distortion has a deficit of low energy photons and a surplus of high energy photons with respect to a blackbody. In this it is like the  $y$  distortion, but the crossover frequency is lower. The “improved” form of the  $\mu$  distortion is plotted in Figure 10.

Finally, at high enough redshift the process of double photon Compton scattering

becomes fast enough to produce the extra photons needed to convert a distorted spectrum into a blackbody. Whenever a photon with frequency  $\nu$  scatters off an electron, there is an impulse  $\propto h\nu/c$  transferred to the electron. This corresponds to an acceleration  $a \propto h\nu^2/(m_e c)$  for a time interval  $\Delta t \propto 1/\nu$ . The energy radiated in new photons is thus  $\propto e^2 h^2 \nu^3 / (m_e^2 c^5)$  which is  $\propto \alpha h\nu (h\nu / (m_e c^2))^2$ . Since the rate of scatterings per photon is  $\propto \Omega_B h^2 (1+z)^3$ , the overall rate of new photon creation is  $\propto \Omega_B h^2 (1+z)^5$  while the Hubble time is  $\propto (1+z)^{-2}$ . Thus the photon creation rate per Hubble time is  $\propto (1+z)^3$  and at earlier enough times a blackbody spectrum is produced no matter how much energy is transferred to the photon field. The emissivity for double photon Compton scattering has approximately the same spectral shape as free-free emission, since both are due to impulsive accelerations. Thus the addition of photons to the radiation field can be described by

$$\frac{\partial n}{\partial y} = A \frac{1 - e^{-x}}{x^3} \left( \frac{1}{e^x - 1} - n \right) \quad (26)$$

where  $A$  is the ratio of photon creation via double photon Compton scattering or free-free emission to the increase of  $y$ . For double photon Compton scattering  $A$  scales like  $(1+z)$ . Because the photons are created primarily at low frequencies,  $n(x)$  approaches a blackbody for  $x \rightarrow 0$ , while the frequency shifts due to Compton scattering are simultaneously transferring photons to larger values of  $x$ .  $A$  is very small at redshifts where distortions can survive, so the photon creation occurs primarily at  $x \ll 1$ . For any  $n = (\exp(x + \mu(x)) - 1)^{-1}$ ,

$$\left( n + n^2 + \frac{\partial n}{\partial x} \right) = -n(n+1) \frac{\partial \mu}{\partial x} \quad (27)$$

so when  $\mu(x) = \mu \exp(-x_0/x)$  and  $x, x_0, \mu$  and  $A$  are all  $\ll 1$ , implying  $n \approx n+1 \approx x^{-1}$ ,

$$x^{-2} \frac{\partial}{\partial x} \left( x^4 \left( n + n^2 + \frac{\partial n}{\partial x} \right) \right) \approx \frac{-\mu \exp(-x_0/x) x_0^2}{x^4} \quad (28)$$

This cancels the  $\partial n / \partial y$  due to photon addition, giving a quasi-equilibrium solution, if  $x_0 = \sqrt{A}$ . With this form for  $n$  one finds a net photon addition rate of

$$\begin{aligned} \frac{\partial N}{\partial y} &= \int x^2 \frac{\partial n}{\partial y} dx \\ &= \int x^2 A \frac{1 - e^{-x}}{x^3} \left( \frac{1}{e^x - 1} - n \right) dx \\ &= A\mu/x_0 = \mu\sqrt{A}. \end{aligned} \quad (29)$$

Since the deficit of photons associated with  $\mu$  is  $\mu\pi^2/3$ , one finds a thermalization rate per unit  $y$  of

$$\frac{\partial \ln \mu}{\partial y} = \frac{3\sqrt{A}}{\pi^2} \propto \sqrt{1+z} \quad (30)$$

Since  $(1+z)\partial y/\partial z \propto \Omega_B h^2 (1+z)^2$ , the overall rate for eliminating a  $\mu$  distortion scales like  $\Omega_B h^2 (1+z)^{5/2}$  per Hubble time. A proper consideration<sup>50</sup> of this interaction of the photon creation process with the Kompaneets equation shows that the redshift from which  $1/e$  of an initial distortion can survive is

$$z_{th} = \frac{4.24 \times 10^5}{[\Omega_B h^2]^{0.4}} \quad (31)$$

which is  $z_{th} = 2.3 \times 10^6$  for the BBNS value of  $\Omega_B h^2$ .

## 8. Summary

So far *COBE* has been a remarkably successful space experiment with dramatic observational consequences for cosmology, and the DIRBE determination of the cosmic infrared background is yet to come. The very tight limits on deviations of the spectrum from a blackbody rule out many non-gravitational models for structure formation, while the amplitude of the  $\Delta T$  discovered by the *COBE* DMR implies a magnitude of gravitational forces in the Universe that is sufficient to produce the observed clustering of galaxies, *but only if the Universe is dominated by dark matter.*

## 9. References

1. Penzias, A. A. & Wilson, R. W. 1965, *ApJ*, **142**, 419.
2. Boggess, N. W. *et al.* 1992, *ApJ*, **397**, 420.
3. Bennett, C. L. *et al.* 1992a. COBE Preprint 92-08, "Recent Results from COBE", to be published in The Third Teton Summer School: The Evolution of Galaxies and Their Environment, eds. H. A. Thronson & J. M. Shull.
4. Hubble, E. 1929, *PNAS*, **15**, 168.
5. Peebles, P. J. E. 1993, "Principles of Physical Cosmology", Princeton University Press.
6. Guth, A. 1981, *Phys. Rev. D*, **23**, 347.
7. Partridge, R. B. & Peebles, P. J. E. 1967, *ApJ*, **148**, 377.
8. Stecker, F. W., Puget, J. L. & Fazio, G. G. 1977, *ApJL*, **214**, L51.
9. Dermott, S. F., Nicholson, P. D., Burns, J. A. & Houck, J. R. 1984, *Nature*, **312**, 505-509.
10. Smoot, G. F. *et al.* 1992, *ApJL*, **396**, L1.
11. Conklin, E. K. 1969, *Nature*, **222**, 971.
12. Kogut, A., Lineweaver, C., Smoot, G. F., Bennett, C. L., Banday, A., Boggess, N. W., Cheng, E. S., De Amici, G., Fixsen, D. J., Hinshaw, G., Jackson, P. D.,

- Janssen, M., Keegstra, P., Loewenstein, K., Lubin, P., Mather, J. C., Tenorio, L., Weiss, R., Wilkinson, D. T., & Wright, E. L., 1993, *ApJ*, **419**, TBD.
13. Harrison, E. R. 1970, *Phys Rev D*, **1**, 2726-2730.
  14. Zeldovich, Ya. B. 1972, *MNRAS*, **160**, 1p.
  15. Peebles, P. J. E. & Yu, J. T. 1970, *ApJ*, **162**, 815-836.
  16. Wright, E. L. *et al.* 1992, *ApJL*, **396**, L13.
  17. Bennett, C. L. *et al.* 1992b, *ApJL*, **396**, L7.
  18. Kogut, A. *et al.* 1992, *ApJ*, **401**, 1-18.
  19. Bennett, C. L., Hinshaw, G., Banday, A., Kogut, A., Wright, E. L., Loewenstein, K. & Cheng, E. S. 1993, *ApJL*, **414**, TBD.
  20. Bennett, D. P., Stebbins, A. & Bouchet, F. R. 1992, *ApJL*, **399**, L5-L8.
  21. Bennett, D. P. & Rhie, S. H. 1993, *ApJ*, **406**, L7.
  22. Sachs, R. K. & Wolfe, A. M. 1967, *ApJ*, **147**, 73.
  23. Bertschinger, E., Dekel, A., Faber, S. M., Dressler, A. & Burstein, D. 1990, *ApJ*, **364**, 370-395.
  24. Holtzman, Jon A. 1989, *ApJSupp*, **71**, 1-24.
  25. Schuster, J., Gaier, T., Gundersen, J., Meinhold, P., Koch, T., Seiffert, M., Wuensche, C. & Lubin P. 1993, *ApJL*, **412**, L47-L50.
  26. Gorski, K. 1992, *ApJL*, **398**, L5-L8.
  27. Lauer, T. & Postman, M. 1992, *BAAS*, **24**, 1264.
  28. Wright, E. L. 1993, *Annals of the New York Academy of Sciences*, **688**, 836.
  29. Crittenden, R., Bond, J. R., Davis, R. L., Efstathiou, G. & Steinhardt, P. J. 1993, *PRL*, **71**, 324-327.
  30. Wright, E. L., Smoot, G. F., Kogut, A., Hinshaw, G., Tenorio, L., Lineweaver, C., Bennett, C. L. & Lubin, P. M. 1994, *ApJ*, **420**, TBD.
  31. Martin, D. H. & Pulett, E. 1970, *Infrared Physics*, **10**, 105-109.
  32. de Bernardis, P., Masi, S., Melchiorri, F., Melchiorri, B. & Vittorio, N. 1992, *ApJ*, **396**, L57-L60.
  33. Watson, R. A., Gutierrez de la Cruz, C. M., Davies, R. D., Lasenby, A. N., Rebolo, R., Beckman, J. E. & Hancock, S. 1992, *Nature*, **357**, 660-665.
  34. Dragovan, Mark, 1993, private communication.
  35. Cheng, E. S., Cottingham, D. A., Fixsen, D. J., Inman, C. A., Kowitt, M. S., Meyer, S. S., Page, L. A., Puchalla, J. L. & Silverberg, R. F. 1993, *ApJ*, **TBD**, TBD.
  36. Gundersen, J., Clapp, A., Devlin, M., Holmes, W., Fischer, M., Meinhold, P., Lange, A., Lubin, P. Richards, P. & Smoot, G. 1993, *ApJ*, **413**, L1.
  37. Meinhold, P., Clapp, A., Devlin, M., Fischer, M., Gundersen, J., Holmes, W., Lange, A., Lubin, P., Richards, P. & Smoot, G. 1993, *ApJL*, **409**, L1-L4.

## Test Case Known Pattern

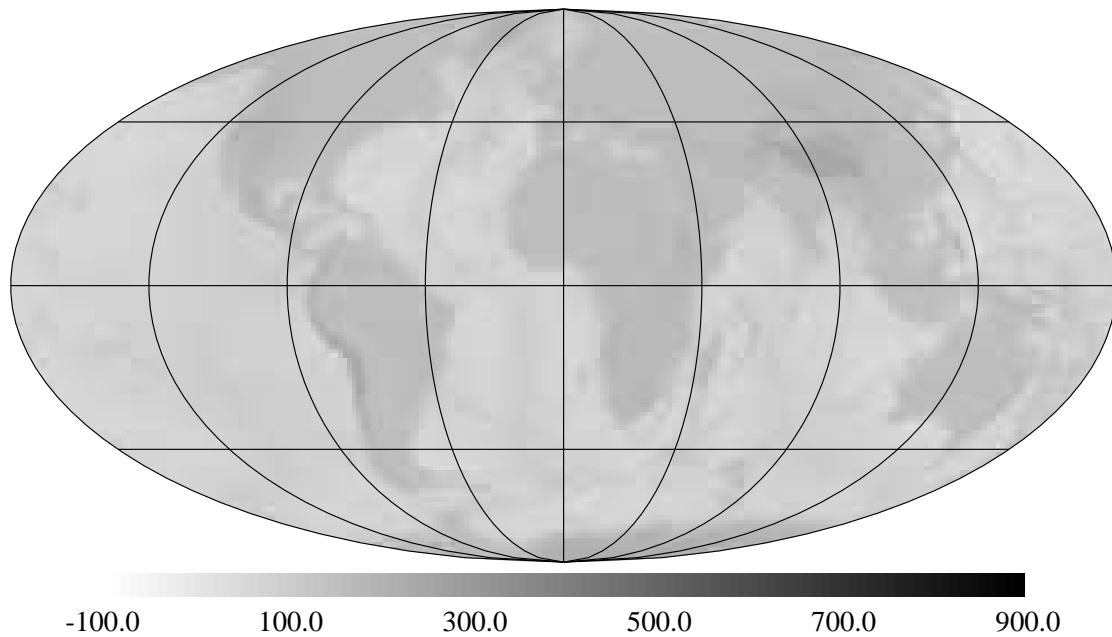


Figure 13: The known pattern used to generate the test case maps.

38. Myers, S. T., Readhead, A. C. S., & Lawrence, C. R. 1993, *ApJ*, **405**, 8-29.
39. Readhead, A. C. S., Lawrence, C. R., Myers, S. T., Sargent, W. L. W., Hardebeck, H. E. & Moffet, A. T. 1989, *Ap. J.*, **346**, 566.
40. Fixsen *et al.* 1994, *ApJ*, **420**, TBD.
41. Mather, J. C. *et al.* 1990, *ApJ*, **354**, L37-L41.
42. Wright, E. L. *et al.* 1991, *ApJ*, **381**, 200-209.
43. Mather *et al.* 1994, *ApJ*, **420**, TBD.
44. Fixsen *et al.* 1994, *ApJ*, **420**, TBD.
45. Wright *et al.* 1994, *ApJ*, **420**, TBD.
46. Walker, T. P., Steigman, G., Schramm, D. N., Olive, K. A. & Kang, H-S. 1991, *ApJ*, **376**, 51-69.
47. Steigman, G. & Tosi, M. 1992, *ApJ*, **401**, 150-156.
48. Kompaneets, A. S. 1957, *Sov. Phys. JETP*, **4**, 730.
49. Zeldovich, Ya. B. & Sunyaev, R. A. 1969, *Ap. & Sp. Sci.*, **4**, 301-316.
50. Burigana, C., De Zotti, G. F., & Danese, L. 1991, *ApJ*, **379**, 1-5.